Journal of Power Electronics (2023) 23:499–509
https://doi.org/10.1007/s43236-022-00557-0

ORIGINAL ARTICLE

Multi-condition dynamic model control strategy of the direct drive motor of electric vehicles based on PIO–LightGBM algorithm

Fang Xie[1,2] · **Wenyu Zhang**[1,2] · **Mengyuan Shen**[1,2] · **Jinqiang Zhang**[1,2]

Received: 12 June 2022 / Revised: 28 October 2022 / Accepted: 30 October 2022 / Published online: 12 December 2022

Abstract
Permanent magnet synchronous motor (PMSM) is widely used in new energy vehicles. At present, to make electric vehicles have a wider speed range, the motor can reach the rated speed above through the field-weakening control. However, when the traditional field-weakening control strategy is above the rated speed, the dynamic response ability of the vehicle declines. Problems such as torque oscillation and current jump occur. To solve these problems, based on a pigeon-inspired optimization (PIO) algorithm and optimized light gradient boosting machine (LightGBM), the dynamic response capability of the permanent magnet synchronous motor is improved. The robust adaptability of the control system to disturbances and parameter changes is also further improved. By collecting experimental data, the importance of relevant variables is analyzed, and the variable with the largest weight is selected as the input of the model. PIO is used to optimize LightGBM, and the loss function is optimized. Finally, the regression model is established. Simulation and experimental results show that the method is effective.

Keywords Pure electric vehicle · Permanent magnet synchronous motor · Fast gradient lifting algorithm · Multiple working conditions · Motor control

1 Introduction

Permanent magnet synchronous motor (PMSM) has the advantages of high power density, high operation efficiency, and good control performance. It is widely used in new energy vehicles [1–3]. Vector control, the most common control method, is realized by current and speed loops and has simple structure and strong reliability [4, 5].

At present, as new energy vehicle motor technology develops, the vehicle drive motor is required to have a wide speed regulation range (output large torque at low speed) and constant power (output at high speed cruise) [6–8]. When the current working point of the motor is far from the predetermined design working point of the controller under different working conditions, such as high speed, low speed, overloading, and underloading, the dynamic response ability of the motor and the steady-state accuracy decrease, resulting in increases in system overshoot and oscillation time [9–12]. Therefore, when the working condition of the motor changes, changing the control parameters of the controller in real time is necessary to ensure the dynamic response ability and steady-state accuracy [13–15].

Vector control is the control strategy of the main drive motor of electric vehicles. Current research on this kind of control strategy mainly focuses on two aspects. The first is to control the motor by building an accurate mathematical model of the motor. Reference [16] designs a real-time inverse system on the basis of OLS-SVM; connects the other original systems in series to form a pseudo linear system, which realizes the linearization and decoupling of the HS-PMSM system; and completes the speed tracking and load torque anti-disturbance control in the width domain. Reference [17] analyzes the relationship between PI regulator parameters and system zeros and poles and puts forward a parameter determination method on the basis of pole assignment. This method can achieve a good control effect when it is used to suppress the resonance of the flexible load system driven by PMSM. However, this method is often unable to cope with high-order nonlinear models,

✉ Fang Xie
06032@ahu.edu.cn

[1] School of Electrical Engineering and Automation, Anhui University, Hefei, China

[2] National Engineering Laboratory of Energy-Saving Motor & Control Technology, Anhui University, Hefei, China

and a change in parameters leads to the decline of control quality. The second aspect current research focuses on is to adaptively match the parameters by introducing intelligent and modern controls. Reference [18] studies the expert PID controller on the basis of expert rules, and the motor speed control performance is significantly improved. Reference [19] designs a high-gain observer on the basis of a feedforward extended nominal mathematical model to quickly track the current and disturbance state and effectively suppress the disturbance caused by speed change. However, this kind of method increases the number of real-time calculations. When the working conditions change, the intelligent selection cannot be rapidly carried out.

Aiming at the reduction of the dynamic response ability of PMSM under different working conditions, this study introduces the controller parameter regression model that is based on pigeon-inspired optimization (PIO)–light gradient boosting machine (LightGBM) algorithm to solve the adverse impact of load change on the expected servo performance of the system under different working conditions [20–22]. By establishing the regression model of control parameters under different working conditions, the motor can match with the parameters under different working conditions, and the dynamic response index is good, so the motor can switch quickly and operate stably under a wide range of working conditions.

Section 2 analyzes the influence of working condition change on motor operation. Section 3 explains the importance of relevant variables by using the fast gradient lifting algorithm with regression modeling. Section 4 builds an experimental platform to verify the theoretical analysis through the experimental results. Section 5 presents a summary.

2 Mathematical model

2.1 Mathematical model of PMSM

The voltage equation of PMSM is.

$$\begin{cases} u_d = R_a i_d + L_d \frac{\mathrm{d}i_d}{\mathrm{d}t} - \omega_e L_q i_q \\ u_q = R_a i_q + L_q \frac{\mathrm{d}i_q}{\mathrm{d}t} + \omega_e L_d i_d + \omega_e \psi_f \end{cases}, \tag{1}$$

where $u_d$andu_q is the component of stator voltage on d-axis and q-axis, respectively; $i_d$andi_q is the component of stator current on d − axis and q − axis, respectively; $L_d$andL_q is the component of stator inductance on d-axis and q-axis, respectively; R_a is the stator resistance;ψ_f is the flux linkage of permanent magnet; n_p is the number of poles of the motor; and ω_e is the electrical angular speed of the motor.

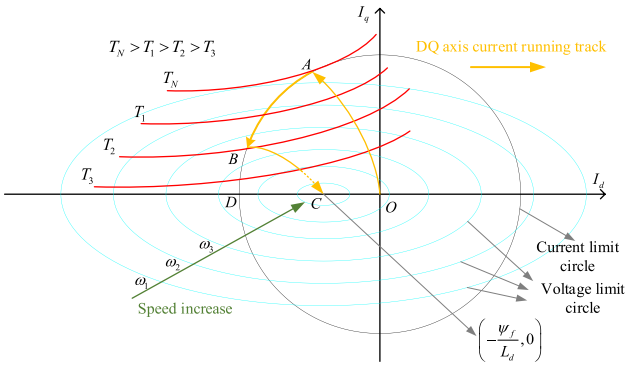

Fig. 1 PMSM electrical constraints

In the control system of PMSM, the inverter has rated voltage u_{smax} and rated current i_{smax} limits. The maximum voltage is related to the DC bus voltage, which can be written as $u_{smax} = u_{dc}/\sqrt{3}$. The working state of the motor meets the following equation:

$$\begin{cases} i_d^2 + i_q^2 \le i_{s\max} \\ u_d^2 + u_q^2 \le u_{s\max} \end{cases}. \tag{2}$$

When PMSM is in steady-state operation, Eq. (1) ignores the resistance voltage drop and differential term, and the voltage balance equation of PMSM can be obtained as follows:

$$\begin{cases} u_d = -\omega_e L_q i_q \\ u_q = \omega_e L_d i_d + \omega_e \psi_f \end{cases}. \tag{3}$$

With Eqs. (2) and (3), the current limit equation and voltage limit equation with i_d and i_q as coordinates can be obtained as follows:

$$\begin{cases} i_d^2 + i_q^2 \le i_{s\max} \\ \left(L_d i_d + \psi_f\right)^2 + \left(L_q i_q\right)^2 \le \left(\frac{u_{dc}}{\sqrt{3}\omega_e}\right)^2 \end{cases}. \tag{4}$$

Equation (4) shows that the current limit equation of PMSM is a circle with (0, 0) as the center that the radius increases in proportion as the current increases, and the radius of current limit circle isI_{smax}. The voltage limit equation of PMSM is an elliptic family with $\left(-\frac{\psi_f}{L_d}, 0\right)$ as the center that long and short radiuses decrease in proportion as speed increases (see Fig. 1).

When the rotating speed is low, the working point of the motor is at point A, and the output torque of the motor is the maximum. As the motor speed exceeds the rated speed and the voltage ellipse shrinks to point C, the d-axis i_d current is required to move to the negative axis. This is the field-weakening control principle based on d-axis current

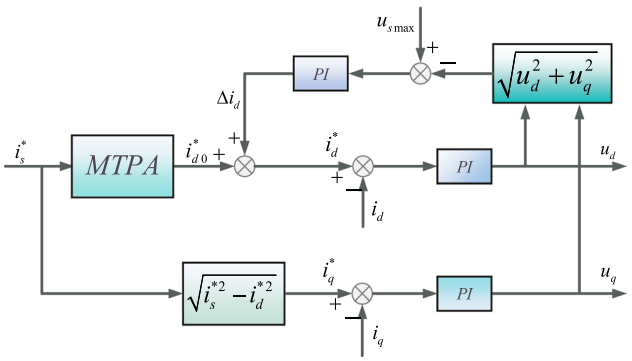

Fig. 2 Flux weakening control block diagram based on d-axis current compensation

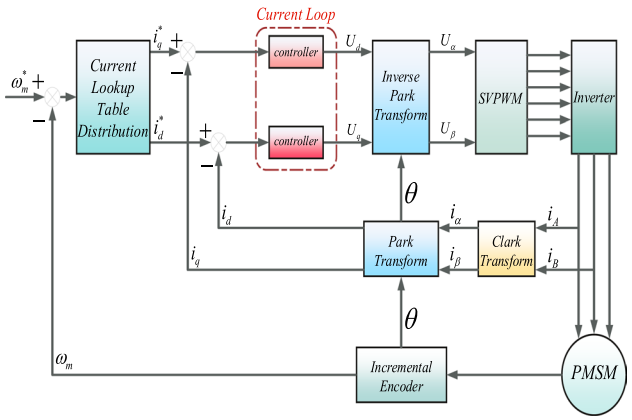

Fig. 3 Vector control system of PMSM

compensation. The control block diagram is illustrated in Fig. 2. The motor works in the field-weakening area. To maintain the maximum output torque, the working point moves along arc AB. When the motor operating point reaches point B, if the speed is further increased, then it should move along arc BC to obtain the maximum torque output. The flux weakening control principle based on d-axis current compensation can only move the working point to the left along the current circle until no intersection exists between the current circle and the voltage circle. In this case, the actual current cannot track the given current, leading to the saturation of the current regulator and control loss of the current.

2.2 Effects of sudden changes in working conditions on torque

The vector control system of PMSM is demonstrated in Fig. 3. ω_m^* is the given angular speed of the motor, and ω_m is the actual angular speed of the motor. i_d^*andi_q^* is the component of given stator current on d-axis and q-axis, respectively. θ is the electrical angle of the motor.

In Fig. 1, with a change in the motor working condition, after the motor enters steady-state operation, currents i_d and i_q fall on curve OAB. In Fig. 3, when the motor speed is lower than the base speed, the control system adopts the maximum torque per ampere control, and point A is the maximum torque output point. When the speed is higher than the base speed, the negative i_d compensation method is adopted for control, corresponding to arc AB in Fig. 1.

With the increasing speed of the motor and limited by the rated voltage u_{smax} and rated current i_{smax} of the inverter, the voltage limit ellipse centered on point C in Fig. 1 shrinks. Apart from the current moves from point A to point B along the circular edge of the current limit circle, the slope of the motor working point increases. When the working point of PMSM gradually approaches the tangent point D of the current limit, i_d changes slightly, whereas i_q changes greatly. This contributes to a large gain of q-axis current loop, which likely increases the fluctuation of current and torque and causes the saturation of the current regulator.

During the actual operation of the motor, its operation under different working conditions, such as high speed, low speed, overloading, and underloading, has an adverse impact on the expected servo performance of the system and causes the instability of the high motor control system and decline of the dynamic response performance index. In addition, the system current, torque oscillation, and regulator saturation in the field-weakening region go wrong. As the traditional controller cannot meet the requirements, this study uses the improved machine learning algorithm to calibrate the controller parameters under various working conditions so that the motor can respond quickly and accurately when its working point changes under different working conditions.

3 Experimental platform construction and importance analysis of measured data

3.1 Platform construction and data acquisition

To quantify the influence of different working conditions on the motor control system, this study uses AVL dynamometer to collect experimental data. Figures 4, 5 present the motor experimental platform and motor console, respectively. Our data are obtained from the AVL bench test of 90 kw electric vehicle PMSM. The motor parameters are displayed in Table 1.

The maximum speed of the motor of the experimental platform in this study reaches 3000 rpm, and the maximum torque is 1500 N·m. First, to analyze the dynamic response ability of the motor under different working conditions, experimental data are collected and verified. Second, the model input and output model are determined by ranking the characteristic importance of experimental data.

Fig. 4 Motor experimental platform

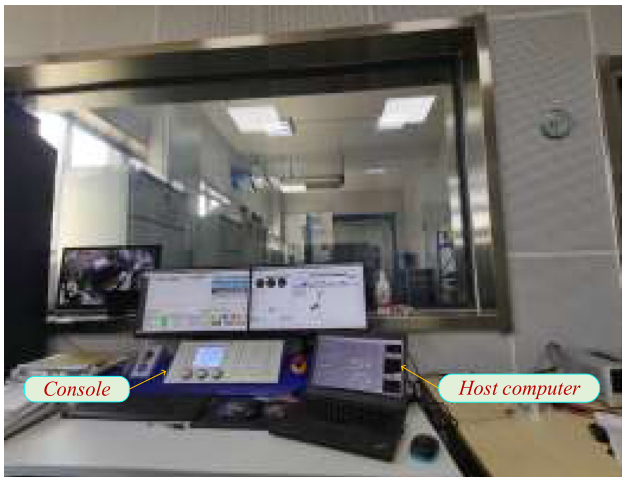

Fig. 5 Motor control platform

Table 1 Motor parameters

Parameter	Value	Symbol
Rated voltage	380	V
Rated current	380	A
Rated power	100	kW
Polar logarithm	6	N/A
Rated speed	1500	rpm
D-axis inductance	0.64	mh
Q-axis inductance	2.12	mh
DC resistance	29.14	mΩ

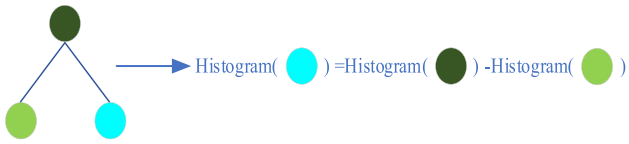

Fig. 6 Training speed of histogram subtraction acceleration model

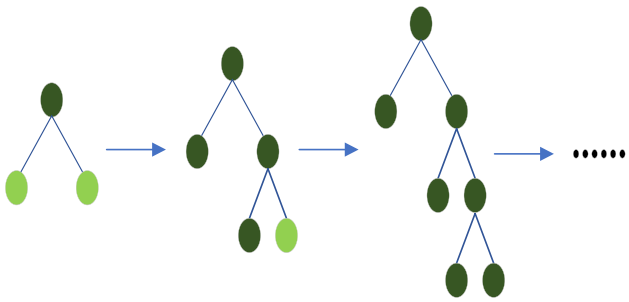

Fig. 7 Level-wise tree growth

3.2 Importance analysis of the relationship between variables and output

LightGBM adopts decision-making tree iterative training to obtain the optimal model and integrates histogram algorithm and leaf wise strategy with depth constraints, as shown in Figs. 6, 7. The algorithm is mostly used for regression and sorting the importance of model features and other tasks. It has the characteristics of small memory and fast running speed.

The data sample input in this research are D_{speed}(rpm), D_{i_d}(V), D_{i_q}(A), $D_{efficiency}$(Percent), D_{torque}(Nm), $D_{frequency}$(Hz), $D_{u_{sd}}$(V), $D_{u_{sq}}$(V), $D_{inputpower}$(W), $D_{outputpower}$(W), $D_{coreloss}$(W), $D_{solidloss}$(W), $D_{mechanicalloss}$(W), $D_{powerfactor}$(%), $D_{totalloss}$(W), and $D_{windingloss}$(W). Among them, the codes of the characteristic quantities of LightGBM corresponding to each input variable are feat1, feat2, feat3, feat4, feat5, feat6, feat7, … and feat16. The output variables are K_p and K_i. The output variable is encoded as feat17. The number of samples is 747 lines; the number of features is 17; the numbers of training and test dataset samples are 626 and 165 lines, respectively.

LightGBM sorting mainly includes the following parts: the data format processing, model training, prediction, feature importance, and leaf node output of samples. Variable importance has two calculation methods, namely, weight (the number of times the variable is used as the partition variable in all trees) and gain (the average gain after the variable is used as the partition variable). This study sets the parameters of LightGBM, such as num_iterations, learning_rate, max_depth, and min_data_in_leaf. By substituting the

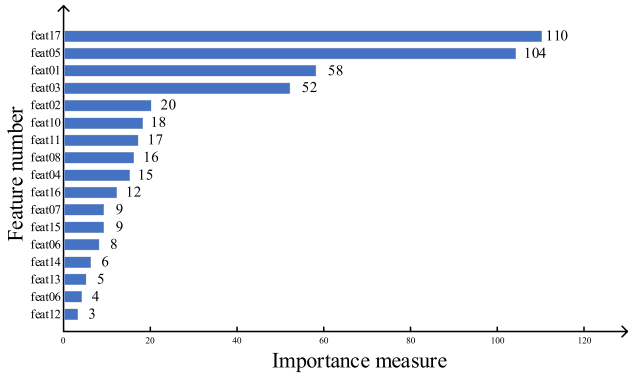

Fig. 8 Importance ranking of characteristic variables based on LightGBM

data into LightGBM for preprocessing, the feature importance of each sample can be acquired, as displayed in Fig. 8.

According to Fig. 8, feat17, feat05, feat01, and feat03 have high influence, and the corresponding variables are K_p, K_i,D_{torque}(Nm), and D_{speed}(rpm). Therefore, the regression modeling input of LightGBM in this study is speed D_{speed}(rpm) and torque D_{torque}(Nm), and the outputs are K_p and K_i.

4 Design of LightGBM multi-condition dynamic model based on PIO algorithm

To improve the dynamic response ability of the motor control system to the change in DQ axis current and ensure motor stability in the full-speed domain, PIO–LightGBM machine learning algorithm is introduced. The controller parameters in the motor full-speed domain are partitioned to improve the limitation of the traditional controller in the nonlinear system.

4.1 Optimization model of LightGBM based on PIO

The LightGBM introduced in this study runs fast and occupies less memory, but the model has many parameters. Inappropriate model parameters directly reduce model prediction accuracy and training speed. To optimize model training, recognition, and prediction on experimental data, PIO algorithm is used to improve LightGBM algorithm. Among them, num_iterations, learning_rate, min_data_in_leaf, and max_depth are optimized. It is also used to improve the flowchart of the LightGBM algorithm, as displayed in Fig. 9. N_{c1} and N_{c2} are the iteration times of compass and landmark operators, respectively.

PIO is an intelligent optimization algorithm that simulates pigeon homing. The mathematical model incorporates compass and landmark operators. The compass operator

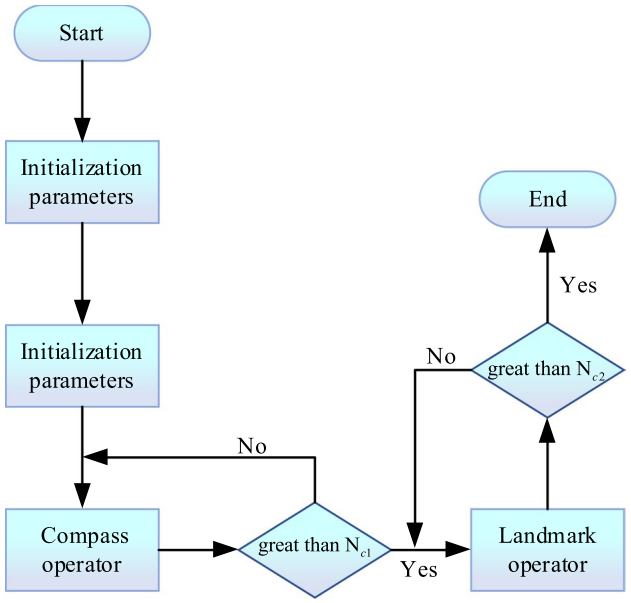

Fig. 9 Algorithm roadmap

is shown in Eq. (5), which initializes pigeon speed and position.

$$\begin{cases} V_i(t) = V_i(t-1) * e^{-Rt} + rand * (X_g - X_i(t-1)) \\ X_i(t) = X_i(t-1) + V_i(t) \end{cases}, \quad (5)$$

where V_i and X_i represent the speed and position of the i-th pigeon, respectively; R is the map factor' Rand is the random number; and t is the pigeon algebra.

The landmark model is established on the basis of pigeons using landmarks for navigation. The landmark operator is presented in Eq. (6) that is if each pigeon can fly a straight distance to the destination.

$$\begin{cases} N_p(t) = \dfrac{N_p(t-1)}{2} \\ X_c(t) = \dfrac{\sum X_i(t) * fitness(X_i(t))}{N_p * \sum fitness(X_i(t))} \\ X_i(t) = X_i(t-1) + rand * (X_c(t) - X_i(t-1)) \end{cases}, \quad (6)$$

where N_p is half the number of pigeons in each generation, $X_c(t)$ is the central position of all pigeons of generation t, and $fitness(x)$ is the mass of each pigeon.

Given that the dataset collected by the experimental platform has unbalanced categories, and the learning of important samples is insufficient, the recognition ability of this sample is inadequate. To deal with the above problems, the LightGBM algorithm is improved. By giving different

weights to different samples, selecting important sample data can easily strengthen algorithm recognition ability. Therefore, modifying the loss function of the algorithm is necessary. To reduce the risk of model overfitting, L_2 regular term is also required. The loss function of the improved mth decision tree is shown in Eqs. (7), (8).

$$L' = -\frac{1}{N}\left(\sum_{i=1}^{N} a_i L(y_i, F_{m-1}(x_i)) + \frac{\lambda}{2}\|a\|_2^2\right), \tag{7}$$

$$a_i = \begin{cases} 1, y_i = 0 \\ \frac{N}{C \cdot N(y_i)}, y_i \neq 0 \end{cases}, \tag{8}$$

where N is the total number of samples; C is the total number of categories; $N(y_i)$ is labeled y_i total number of samples; a_i is the category weight coefficient; $L(y_i, F_{m-1}(x_i))$ is the original loss function; $F_{m-1}(x_i)$ is the predicted value given by the model composed of the first M-1 decision trees under the condition of input x_i; λ is the regularization coefficient; $y_i = 0$ represents the important sample label, and the sample weight is reset to 1; and $y_i \neq 0$ stands for other sample labels, and the sample weight is determined by N, C, and $N(y_i)$.

4.2 Multi-condition dynamic model based on PIO–LightGBM algorithm

A 3D graph with X-axis as speed, Y-axis as torque, and z-axis as K_p and K_i is created. To avoid the phenomenon of motor output torque oscillation and current ripple caused by the continuous switching of controller parameters, the output of the return model is divided into sections. The interval division is determined according to the output and change degree of z-axis. The interval with a huge change in z-axis is intensively discretized, whereas the interval with a small change in z-axis is loosely discretized. Then, the median value of the discrete z-interval is taken. It is at the point corresponding to the regression model to divide the size of the corresponding XOY plane square interval. Furthermore, a dead zone in each interval is set to prevent the repeated switching of controller parameters. The regression block diagram of the controller based on PIO–LightGBM is shown in Fig. 10.

In Fig. 10, with a large number of experimental tests in the motor full-speed domain, a large amount of sample data are regressed and analyzed according to the PIO– LightGBM algorithm, and the parameters are sent to the controller according to different torques and speeds. In addition, as the loss degree function is set, the model output parameters slightly differ under the same condition. Hence, whether the model must be adjusted according to the loss degree function should be determined.

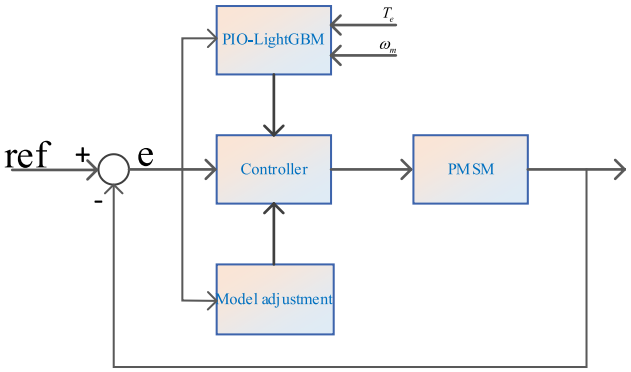

Fig. 10 Control block diagram based on PIO–LightGBM

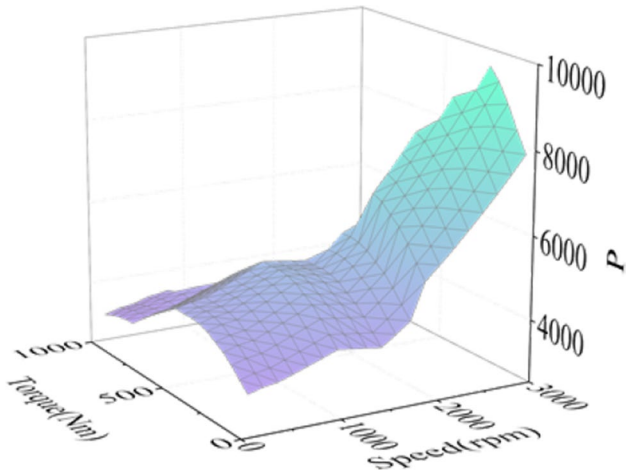

Fig. 11 P value regression

4.3 Simulation platform construction

According to the analysis in Sect. 3, collecting and calculating feat05, feat01, and feat17 in the motor full-speed domain are necessary to expand the full-speed domain of the efficient control of the motor and realize the multi-working condition and efficient control strategy of the motor. Therefore, the regression model based on PIO–LightGBM is constructed by collecting experimental data, and each region corresponds to a controller parameter. First, different motor speeds are given, and then different load torques are applied to record torque and speed data. Next, the dynamic response capabilities of different control methods are compared. Finally, the feasibility and rapidity of the control method based on PIO–LightGBM algorithm are verified.

With appropriate experimental data as required, PIO–LightGBM algorithm is used to model the regression of controller parameters. The graphs of P- and I-values with respect to speed and torque are revealed in Figs. 11, 12, respectively.

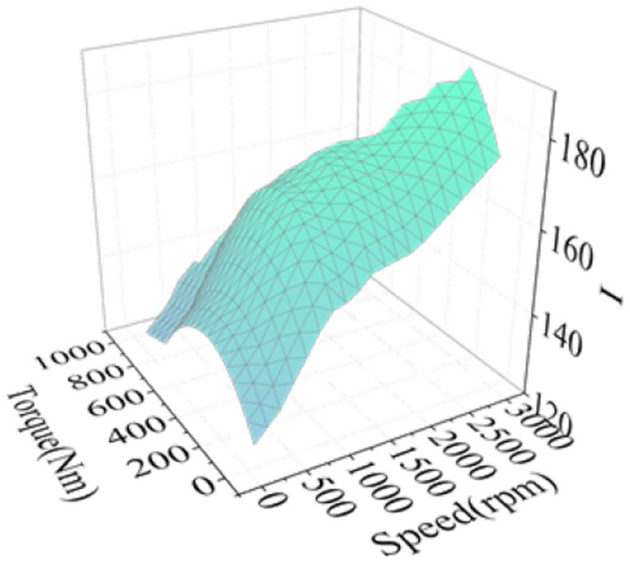

Fig. 12 *I* value regression

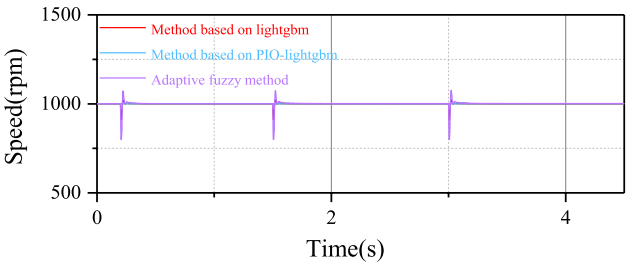

Fig. 13 Speed waveform

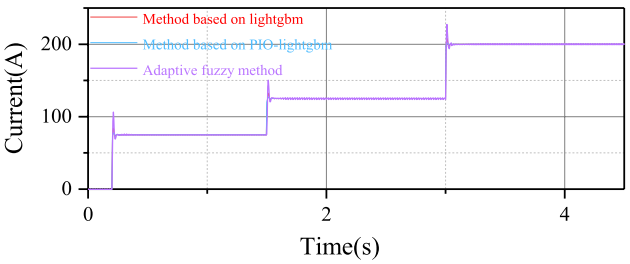

Fig. 14 Q-axis current waveform

To prove the feasibility of the method, a simulation model is built to verify it. We set the motor speed to 1000 rpm, add 300 N·m in 0.2 s, 500 N·m in 1.5 s, and 800 N·m in 3 s. The experiment uses three control methods to compare, which are method one of purple curve that is based on adaptive fuzzy control method. Method 2 of red curve is based on LightGBM control method. Method 3 of blue curve is based

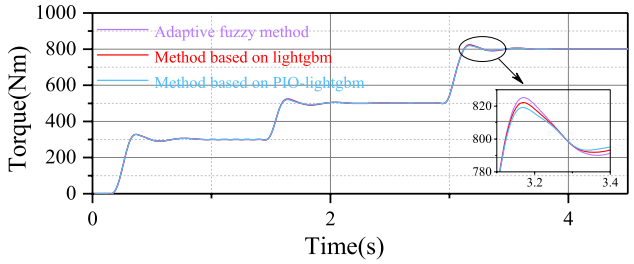

Fig. 15 Torque waveform

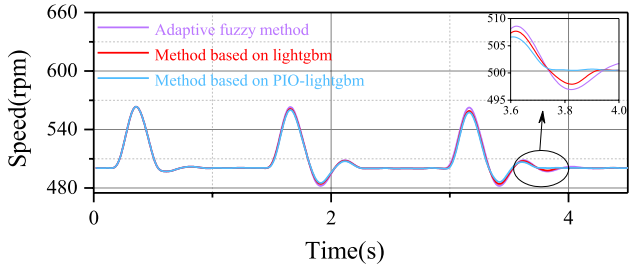

Fig. 16 Speed waveform

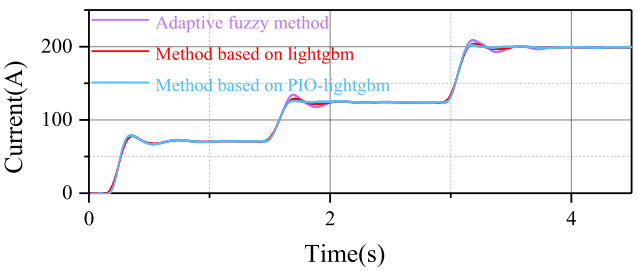

Fig. 17 Q-axis current waveform

on PIO–LightGBM control method. The following figure shows the corresponding torque speed waveform.

Figure 13 shows the speed waveform, and Fig. 14 shows the q-axis current waveform. The traditional method has a large overshoot and a long adjustment practice, whereas the method in this study has a small overshoot and a short adjustment time.

4.4 Analysis of experimental results

To verify the effectiveness of the regression model, we set up a laboratory platform for the following tests. The experiment is divided into two working conditions:high load with medium low speed as well as low load with high speed. When the motor speeds are 500, 1000, 1500, 2000, and 3000 rpm, different load torques are applied to analyze the dynamic response ability of the three control methods.

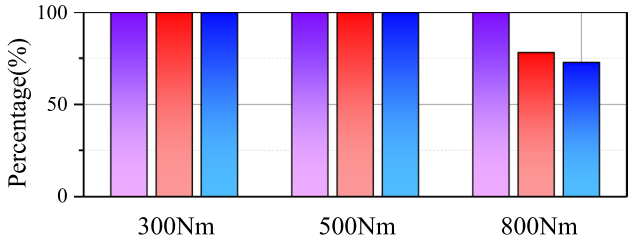

Fig. 18 Torque comparison diagram

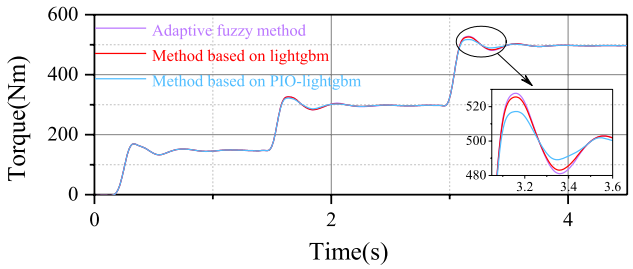

Fig. 19 Torque waveform

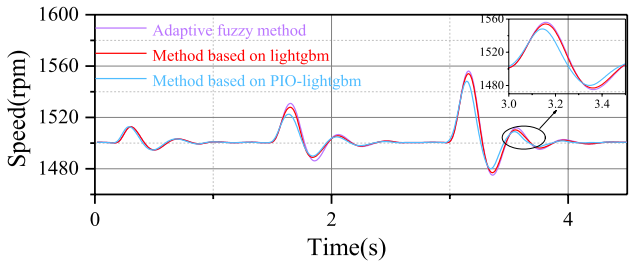

Fig. 20 Speed waveform

(1) The speed is 500 rpm.

We add 300 N·m in 0.2 s, 500 N·m in 1.5 s, and 800 N·m in 3 s. The corresponding torque waveform is illustrated in Fig. 15, and the speed waveform is exhibited in Fig. 16. The q-axis current waveform diagram is shown in Fig. 17, and the torque comparison diagram of various methods is shown in Fig. 18. Based on the purple curve, when the speed is 500 rpm and the torque is 300 N·m and 500 N·m, the three control methods have the same effect. When the torque is 800 N·m, in the case of low torque, the control effects of the three methods are similar. In the case of high torque, the overshoot of torque for method three is 23% lower than method 1 and 12% lower than method 2. The overshoot of Method 3 is smaller, and the motor speed reaches stability faster.

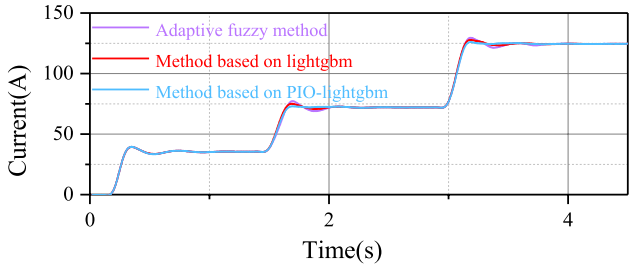

Fig. 21 Q-axis current waveform

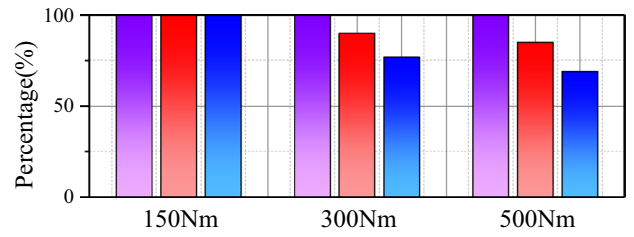

Fig. 22 Torque comparison diagram

(2) The speed is 1500 rpm.

We add 150 N·m in 0.2 s, 300 N·m in 1.5 s, and 500 N·m in 3 s. The corresponding torque waveform is demonstrated in Fig. 19, and the speed waveform is shown in Fig. 20. The q-axis current waveform diagram is shown in Fig. 21, and the torque comparison diagram of various methods is shown in Fig. 22. Based on the purple curve, when the speed is 1500 rpm and the torque is 150 N·m, the three control methods have the same effect. When the torque is 300 N·m, the overshoot of method 3's torque is 25% lower than that of method 1, and method 2's torque is 11% lower than that of method 1. When the torque is 500 N·m, the amount of overshoot in method 3's torque is 35% lower than that of method 1 and 15% lower than that of method 2. The motor speed applying Method 3 is smoother and less volatile.

(3) The speed is 3000 rpm.

We add 125 N·m in 0.2 s and 240 N·m in 1.8 s. The corresponding torque waveform is displayed in Fig. 23, and the speed waveform is shown in Figs. 24, 25. The applicable comparison diagram of various methods is shown in Fig. 26. When the speed is 3000 rpm, the torque is 125 N·m, the overshoot of method 3's torque is 37% lower than that of method 1, and method 2's torque is 32% lower than that of method 1. When the torque is 240 N·m, the torque overshoot of method 3 is 34% lower than that of method 1, and that of method 2 is 24% lower than that of method 1. The system is more stable.

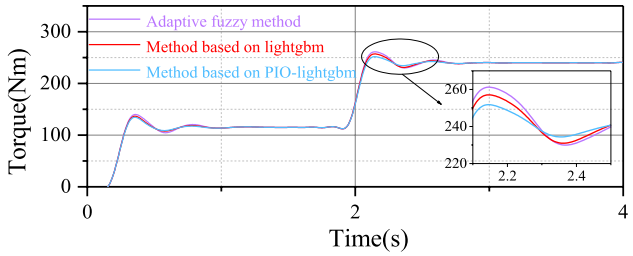

Fig. 23 Torque waveform

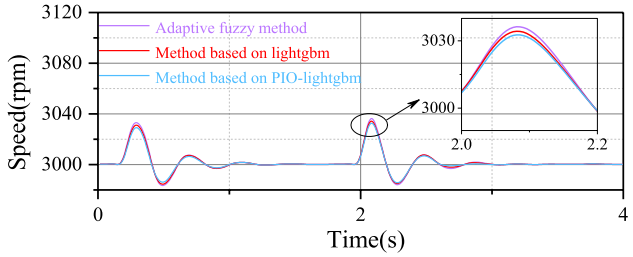

Fig. 24 Speed waveform

(4) The speed is 2000 rpm to 500 rpm.

We keep the torque at 400 N·m unchanged and reduce the speed from 2000 to 500 rpm when the time is 0.2 s. The corresponding speed waveform is shown in Fig. 27, the d-axis current waveform is shown in Fig. 28, and the torque comparison diagram of various methods is shown in Fig. 29. The overshoot of method 3 is 17% lower than that of method 1, and that of method 2 is 8% lower than that of method 1.

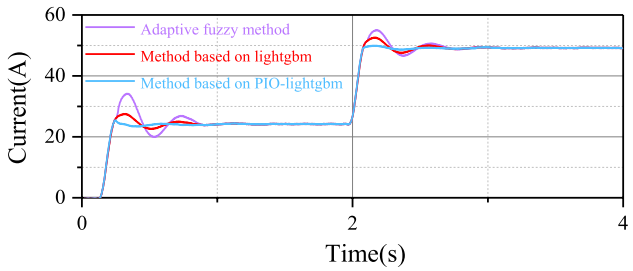

Fig. 25 Q-axis current waveform

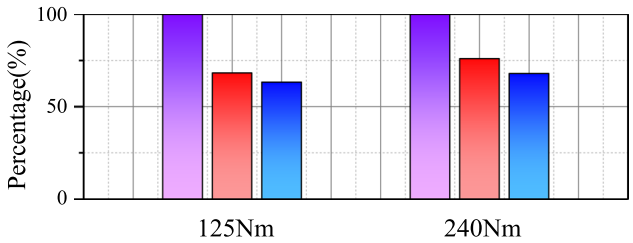

Fig. 26 Torque comparison diagram

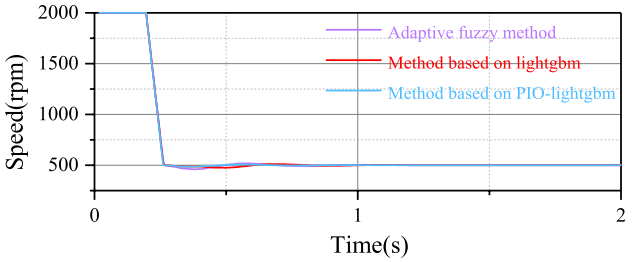

Fig. 27 Speed waveform

Figures 15–29 illustrate that the control method based on PIO–LightGBM algorithm has better dynamic performance than traditional and adaptive fuzzy controls under low speed and high torque conditions and medium and high speed conditions. Compared with the two other control systems, the response time of the motor based on PIO–LightGBM algorithm is shorter, and the control time based on PIO–LightGBM algorithm is more robust to the load change.

5 Conclusion

In this study, an optimal control strategy based on PIO–LightGBM algorithm is proposed for field-weakening control of permanent magnet synchronous motor. The current limit circle and voltage limit circle are established when the motor is above the rated speed. The influence of minor changes in d-axis current on q-axis current is analyzed. On this basis, the experimental data are collected,

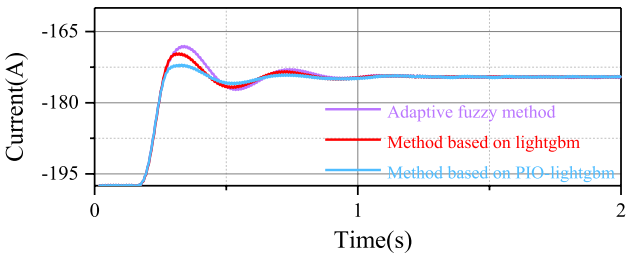

Fig. 28 D-axis current waveform

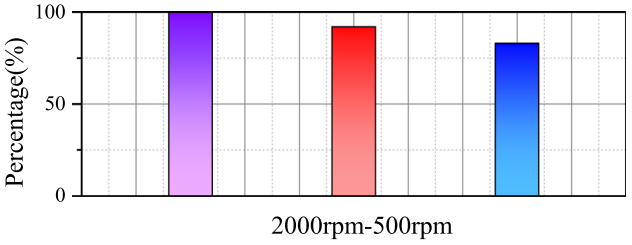

Fig. 29 Speed comparison chart

the importance of relevant variables is analyzed, and the optimal control strategy based on PIO–LightGBM algorithm is proposed, in which the speed and torque are taken as the input and the controller parameters as the output. Finally, the simulation results show that the prediction of the controller parameters meets the requirements of motor operation. In addition, in view of the nonlinear characteristics of the motor system, the PIO–LightGBM algorithm is adopted for multiple working conditions and efficient control strategy, which improves the dynamic response ability of the motor under a wide range of working conditions. In the future, the proposed scheme may be extended to further improve the dynamic performance of the motor.

Acknowledgements This work was supported by Natural Science Foundation of Anhui Province (2108085ME179) and National Natural Science Foundation of China (51607002).

Data Availability The data that support the findings of this study are available from the corresponding author upon requests.

References

1. Meesala, R.E.K., Athikkal, S., Aruldavid, R.: Improved direct torque controlled PMSM Drive for electric vehicles. J. Inst. Eng. India Ser. B **103**, 1177–1188 (2022). https://doi.org/10.1007/s40031-022-00716-8
2. Zhu, S., Zhang, H.: Simplified model predictive current control strategy for open-winding permanent magnet synchronous motor drives. J. Power Electron. **21**, 911–920 (2021). https://doi.org/10.1007/s43236-021-00237-5
3. Deng, X., Li, M., Xu, M.: Sensorless control of printed permanent magnet synchronous motor. J. Power Electron. (2022). https://doi.org/10.1007/s43236-022-00521-y
4. Zhang, Z., Chen, Y., Feng, X., et al.: Linear active disturbance rejection speed control with variable gain load torque sliding mode observer for IPMSMs. J. Power Electron. **22**, 1290–1301 (2022). https://doi.org/10.1007/s43236-022-00429-7
5. Liu, Z.-H., Nie, J., Wei, H.-L., Chen, L., Li, X.-H., Lv, M.-Y.: Switched PI control based MRAS for sensorless control of PMSM drives using fuzzy-logic-controller. IEEE Open J. Power Electron. **3**, 368–381 (2022). https://doi.org/10.1109/OJPEL.2022.3182053
6. Qian, X., Xiaorui, G., Haihong, Q., Ying, Z., Yaowen, D.: Research on the application of flux-weakening control in PMSM with wide range speed variation. Int. Conf. Smart Grid Electr Automation (ICSGEA) **2017**, 371–374 (2017). https://doi.org/10.1109/ICSGEA.2017.32
7. Ping, L., Lan, C.: Study on controlling and simulation of drive system for permanent magnet synchronous motor in electrical vehicle. Power Eng. Automation Conf. **2012**, 1–4 (2012). https://doi.org/10.1109/PEAM.2012.6612509
8. J. Wang, J. Wu, C. Gan and Q. Sun, "Comparative study of flux-weakening control methods for PMSM drive over wide speed range," 2016 19th International Conference on Electrical Machines and Systems (ICEMS), 2016, pp. 1–6.
9. Sant, A.V., Rajagopal, K.R.: PM synchronous motor speed control using hybrid fuzzy-pi with novel switching functions. IEEE Trans. Magn. **45**(10), 4672–4675 (2009). https://doi.org/10.1109/TMAG.2009.2022191
10. Wang, A., Jia, X., Dong, S.: A new exponential reaching law of sliding mode control to improve performance of permanent magnet synchronous motor. IEEE Trans. Magn. **49**(5), 2409–2412 (2013). https://doi.org/10.1109/TMAG.2013.2240666
11. Kuznetsov, V.E., Lukichev, A.N., Chung, P.T.: Speed control of permanent magnet synchronous motor with voltage surges reduction by means of adaptive control. IEEE Conf. Russian Young Res. Electr. Electron. Eng. (EIConRus) **2019**, 590–594 (2019). https://doi.org/10.1109/EIConRus.2019.8657032
12. Li, Z., Zhou, S., Xiao, Y., Wang, L.: Sensorless vector control of permanent magnet synchronous linear motor based on self-adaptive super-twisting sliding mode controller. IEEE Access **7**, 44998–45011 (2019). https://doi.org/10.1109/ACCESS.2019.2909308
13. Alfehaid, A.A., Strangas, E.G., Khalil, H.K.: Speed control of permanent magnet synchronous motor with uncertain parameters and unknown disturbance. IEEE Trans. Control Syst. Technol. **29**(6), 2639–2646 (2021). https://doi.org/10.1109/TCST.2020.3026569
14. Nguyen, T.H., Nguyen, T.T., Nguyen, V.Q., Le, K.M., Tran, H.N., Jeon, J.W.: An adaptive sliding-mode controller with a modified reduced-order proportional integral observer for speed regulation of a permanent magnet synchronous motor. IEEE Trans. Industr. Electron. **69**(7), 7181–7191 (2022). https://doi.org/10.1109/TIE.2021.3102427
15. Nguyen, A.T., Rafaq, M.S., Choi, H.H., Jung, J.: A model reference adaptive control based speed controller for a surface-mounted permanent magnet synchronous motor drive. IEEE Trans. Industr. Electron. **65**(12), 9399–9409 (2018). https://doi.org/10.1109/TIE.2018.2826480
16. He, Y., Wang, Z., Zheng, S.: "Decoupling control of high speed permanent magnet synchronous motor based on online least squares support vector machine inverse system method. Proc. CSEE **36**, 5639–5646 (2016)
17. Ding, Y., Xiao, X.: "Parameter tuning methods based on pole placement for PI controllers of flexible loads driven by PMSM. Proc. CSEE **37**, 1225–1239 (2017)
18. Shi, J., Liu, Y.: "Simple expert PID speed control of ultrasonic motors. Proc. CSEE **33**, 120–125 (2013)
19. Ke, D., Wang, F., Li, J.: Predictive current control of permanent magnet synchronous motor based on an adaptive high-gain observer. Proc. CSEE. **41**, 728–738 (2021)
20. Ju, Y., Sun, G., Chen, Q., Zhang, M., Zhu, H., Rehman, M.U.: A model combining convolutional neural network and LightGBM algorithm for ultra-short-term wind power forecasting. IEEE Access **7**, 28309–28318 (2019). https://doi.org/10.1109/ACCESS.2019.2901920
21. G. Ke et al., "LightGBM: A highly efficient gradient boosting decision tree", Proc. Adv. Neural Inf. Process. Syst., pp. 3146–3154, 2017.
22. Friedman, J.H.: Greedy function approximation: a gradient boosting machine. Ann. Statist. **29**(5), 1189–1232 (2001)

Fang Xie was born in 1977. She received her Ph.D. degree in circuits and systems from the Anhui University, Hefei, China in 2015. She is currently a Professor with the School of Electrical Engineering and Automation, Anhui University. Her research focuses on motor controlling and power electronic technology.

Mengyuan Shen received his B.S. degree in building electrical and intelligent from Anhui University of Science and Technology in Bengbu, China in 2019, where he is currently working toward his M.S. degree in motor control. His current research interests include advanced control of induction motor drive and control of permanent magnet synchronous motor drives.

Wenyu Zhang was born in July 1998. He is currently working toward his master's degree in electrical engineering with the School of Electrical Engineering and Automation, Anhui University, Hefei, China. His research interests include motor control and motor control system design.

Jinqiang Zhang received his B.S. degrees in electrical engineering and automation in 2019 from the Chaohu University, Hefei, China, where he is currently working toward his master's degree in motor control. His current research focuses on advanced control of AC motor drive.